Wind Sea behind a Cold Front and Deep Ocean Acoustics

W. E. FARRELL,[a] J. BERGER,[b] J.-R. BIDLOT,[c] M. DZIECIUCH,[b] W. MUNK,[b] R. A. STEPHEN,[d] AND P. F. WORCESTER[b]

[a] *Del Mar, California*
[b] *Scripps Institution of Oceanography, La Jolla, California*
[c] *European Centre for Medium-Range Weather Forecasting, Reading, United Kingdom*
[d] *Woods Hole Oceanographic Institution, Woods Hole, Massachusetts*

(Manuscript received 16 November 2015, in final form 7 March 2016)

ABSTRACT

A rapid and broadband (1 h, $1 < f < 400$ Hz) increase in pressure and vertical velocity on the deep ocean floor was observed on seven instruments comprising a 20-km array in the northeastern subtropical Pacific. The authors associate the jump with the passage of a cold front and focus on the 4- and 400-Hz spectra. At every station, the time of the jump is consistent with the front coming from the northwest. The apparent rate of progress, 10–20 km h^{-1} (2.8–5.6 m s^{-1}), agrees with meteorological observations. The acoustic radiation below the front is modeled as arising from a moving half-plane of uncorrelated acoustic dipoles. The half-plane is preceded by a 10-km transition zone, over which the radiator strength increases linearly from zero. With this model, the time derivative of the jump at a station yields a second and independent estimate of the front's speed, 8.5 km h^{-1} (2.4 m s^{-1}). For the 4-Hz spectra, the source physics is taken to be Longuet-Higgins radiation. Its strength depends on the quantity $F_\xi^2 I$, where F_ξ is the wave amplitude power spectrum and I the overlap integral. Thus, the 1-h time constant observed in the bottom data implies a similar time constant for the growth of the wave field quantity $F_\xi^2 I$ behind the front. The spectra at 400 Hz have a similar time constant, but the jump occurs 25 min later. The implications of this difference for the source physics are uncertain.

1. Introduction

Fluctuations in pressure and vector velocity (collectively, acoustics) in the deep ocean are driven by processes on the ocean surface, absent anthropogenic, biologic, or seismic sources. At frequencies in the range $1 < f < 10$ Hz, the sound is attributable to radiation from nonlinear interactions between oppositely directed gravity waves of half the frequency (Farrell and Munk 2010). We call this Longuet-Higgins (L-H) radiation, although the theory was developed to explain microseisms, which have much lower frequency (Longuet-Higgins 1950; Hasselmann 1963).

For frequencies greater than about 10 Hz, the wind-correlated acoustic signal cannot be due to the L-H mechanism, given accepted models of the shortwave spectrum (Farrell and Munk 2013). Goncharov (1970) invoked nonlinear interactions between gravity waves and turbulence, which might be effective at frequencies of a few tens of hertz. At hundreds of Hertz, processes related to the creation and destruction of bubbles and clouds of bubbles have been proposed (Oguz 1994; Deane and Stokes 2010).

Since Knudsen (1948), there have been many papers relating ocean sound to overhead wind. Most studies of deep ocean acoustics have taken averages of spectra based on measured or estimated overhead wind (e.g., Duennebier et al. 2012). Small-scale studies in the laboratory or at shallow depths in the ocean have measured near-field radiation from breaking wave events. It is not obvious how this work could connect to deep observations, which are receptive to surface conditions over distances many times the measurement depth.

Our approach is to examine in detail a single acoustic event observed during the 2013 Ocean Bottom Seismometer Augmentation in the North Pacific (OBSANP) experiment in the northeastern subtropical Pacific (Stephen et al. 2014). A similar approach, but with

Denotes Open Access content.

Corresponding author address: W. E. Farrell, 13765 Durango Dr., Del Mar, CA 92014.
E-mail: wef@farrell-family.org

DOI: 10.1175/JPO-D-15-0221.1

hurricane-force winds in the Atlantic, was taken by Wilson and Makris (2006).

2. Observations

a. Instruments

During the OBSANP experiment (19 June–3 July 2013), nearly two score instruments were deployed both on the ocean floor (5000 m) and up a vertical line array (VLA), reaching 1000 m above the bottom (Fig. 1; Stephen et al. 2014). Here we discuss a few hours of data taken on 1 July (Julian day 182) from seven systems (R. A. Stephen and P. F. Worcester 2014, unpublished data).

The acoustic data of the long-period (LP) systems were acquired by a novel hydrophone [Science Applications International Corporation (SAIC), now Leidos]. This hydrophone, not a commercial product, is based on a sensitive amplifier and a Channel Technologies Group ITC-1175 transducer. Its theoretical noise floor is about 20 dB below that of the High Tech, Inc., (HTI) HTI-90-U at 100 Hz. The LP systems also carried a Nanometrics T240 seismometer. The data of the short-period (SP) systems were acquired on High Tech, Inc., HTI-90-U hydrophones and Sercel L28B geophones (4.5-Hz resonant frequency). The VLA hydrophone data are not discussed here.

b. Overview

In the 1–10-Hz band, when the overhead wind is stronger than about 6 m s^{-1}, sound in the deep ocean is almost invariant (McCreery et al. 1993). This is taken to indicate that, at any wave frequency $0.5 < f_w < 5$ Hz ($6.5 < \lambda < 0.06$ m), the wavenumber spectrum under these conditions is both isotropic in direction and also constant in amplitude. Slighter winds lead to a decrease in the acoustic spectrum. These so-called busts have been attributed to changes in the directional spread of the waves (Farrell and Munk 2010). Busts have been known for at least two decades (Dorman et al. 1993).

Acoustic fluctuations at a frequency of 4 Hz are particularly favorable for inferring conditions on the ocean surface. Although useful information can also be gleaned from the 5–10-Hz octave, the spectrum here is plagued by ship noise. On the low side of 4 Hz, the wave field is frequently a mixture of wind sea and swell, and acoustic spectra cannot distinguish between the two.

Figure 2 shows 2-week histories of the observed 4-Hz spectral estimates for pressure and vertical velocity at the seven OBSANP stations. Our focus is the bust during interval AB, and, in particular, the recovery from the bust at point B, as displayed in the middle and bottom panels.

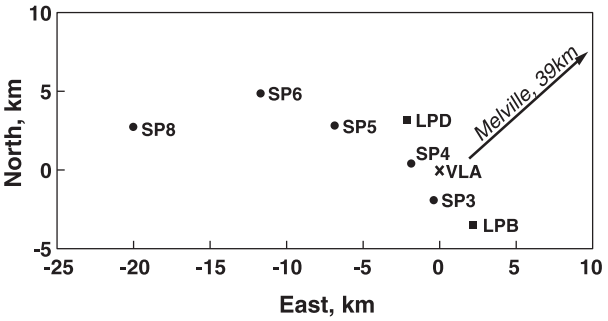

FIG. 1. The seven selected OBSANP stations spanned 20 km in the east–west direction. The VLA location (cross; 33.42°N, 137.68°W) marks the origin. For the crucial hour of analysis (0700–0800 UTC), the R/V *Melville* was some 39 km to the northeast, heading directly toward the VLA at 2 m s^{-1}.

The values of the 4-Hz spectra for the SAIC hydrophones at LPB (dark red) and LPD (red) are nearly identical and fall to the lowest levels in the first bust on Julian day-of-year (DOY) 172. The HTI hydrophones on the other 5 systems are clearly limited by self-noise. There is a profound difference in the data from the two sensor types during the first 5 days of the record, but this is not as serious a defect for the AB bust, which was shallower.

For any time window, the nominal 4-Hz pressure and velocity spectra vary from sensor to sensor, and amplitude correction factors are introduced to obtain the superposition illustrated in the figure. The efficacy of these corrections is apparent in the lower two panels over the 7 h following label B. Section 6d has a discussion of these empirical factors.

Wind speed U and direction at Research Vessel (R/V) *Melville* were recorded by a bow sensor, 26 m above the water, and corrected for ship motion. Between times A and B, the ship was towing an acoustic source and twice passed through the array. The first crossing was at 181.431 (1000 UTC), the second at 182.743 (1750 UTC). At time B, the ship was about 39-km away and heading straight toward the VLA (Fig. 1). At this time, the ship's wind record shows an abrupt jump in the wind speed of about 5 m s^{-1} (Fig. 3).

Attributing the acoustic field at this frequency to nonlinear surface gravity wave interactions, L-H radiation, it can be modeled as arising from a surface layer of incoherent dipoles (Brekhovskikh 1966; Guralnik et al. 2013). It follows that 90% of the acoustic power arises from within a disk of ocean surface with a radius 3 times the observation depth, in this case some 15 km. Thus, R/V *Melville* was in the far field for most of interval AB. But the near synchrony between the wind change and the acoustic change suggests the ship's measurement was representative of the wind field over a patch of ocean

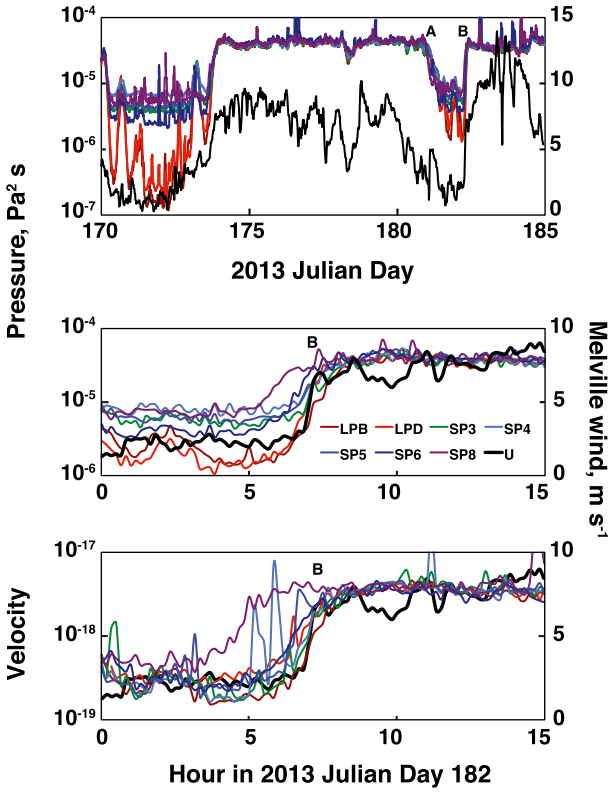

FIG. 2. (top) The 4-Hz spectral estimates of pressure are nearly independent of wind in the middle week when the speed rarely dropped below 6 m s^{-1}. This span is bracketed by busts. The spectra have been equalized to obtain superposition during the intervals with high winds. For the hours surrounding time B, (middle) the spectra of pressure and (bottom) vertical velocity [(m s^{-1})^2 s] show the acoustic jump varies with location and is more gradual than the jump in the wind. The legend in (middle) shows the color coding for the 7 stations. The wind in (top) is smoothed over 1 h, and, in the others, 10-min smoothing was applied.

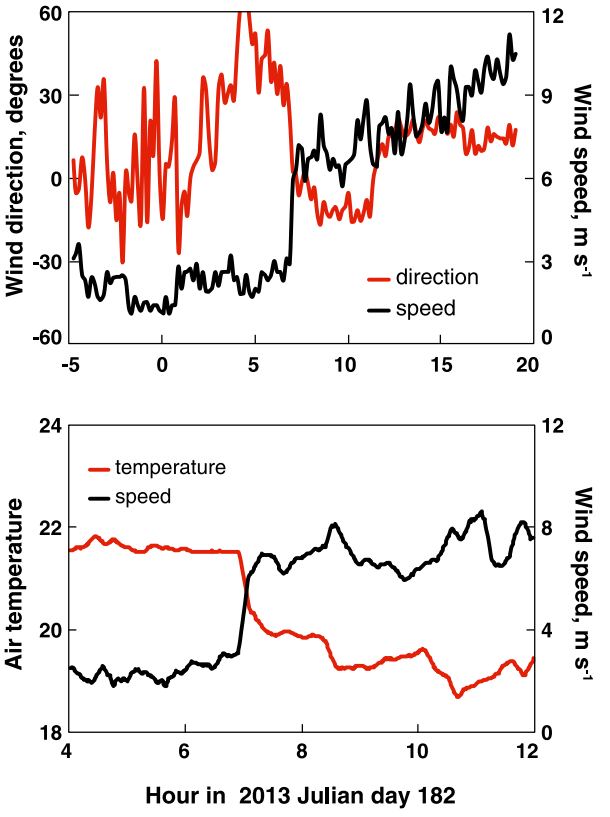

FIG. 3. At the time of the jump in wind speed, 0700 UTC, (top) the direction rotated 45° and (bottom) the temperature dropped almost 2°. The directions are measured upwind, so the rotation was counterclockwise.

surface at least as large as its distance from the array. The jump in U was not just a phenomenon restricted to the R/V *Melville* location.

The suite of meteorological observations at R/V *Melville* is consistent with the jump in the wind at 0700 UTC being due to the passage of a cold front (Fig. 3). Meteorological models for the weather on this day confirm a front did pass overhead, moving toward the southeast, as is typical.

c. Weather

The European Centre for Medium-Range Weather Forecasts (ECMWF) forecast model of the regional weather during OBSANP shows that a cold front moved over the array, trending in a southeasterly direction, somewhat before 1200 UTC, 1 July 2013 (Julian day 182). The synoptic weather situation was such that about 10° to the north of the OBSANP location, a primary low-pressure system was weakening but stationary, forcing a distinctive cold air descent that reached the array on 1 July at about 0800 UTC with strong winds and wind-sea generation (see also Fig. 3). Moreover, the model shows that, before the front's passage, there was an extensive area of negligible wind sea (a consequence of low wind speed) over the array and extending to the east. This corresponds precisely with the profound depression in the acoustics ahead of the front.

The ECMWF system assimilates a vast amount of meteorological data, including a variety of satellite measurements, and in addition is coupled to an ocean wave model. It produces two forecasts per day from the 0000 and 1200 UTC analyses. The spatial resolution of the atmospheric model is 16 km, and for the wave model it is 28 km. The wave field is calculated for discrete frequency/direction bins. There are 36 directions, and the logarithmic frequency bins extend up to 1 Hz (Janssen 2008; ECMWF 2015). For this study, the forecast was initialized from the state at 0000 UTC 1 July and the hourly output analyzed through the day. It is necessary to use the forecasts, since the model analysis is only

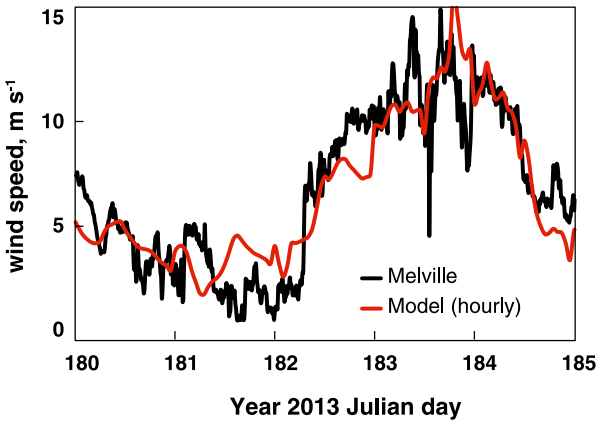

FIG. 4. The red curve shows the collated 10-m wind from the ECMWF short-range hourly forecast output (0000–1100 UTC) based upon the 0000 and 1200 UTC analyses. The wind has been interpolated onto the R/V *Melville* track and agrees, in general, with the measured wind. The jump (0800 UTC, day 182) associated with the front, however, is shallower than the recorded jump and about 2 h later. Generally, the difference in the ECMWF wind between the R/V *Melville* course and the fixed VLA position is small, but at times reaches an hour or so.

computed every 6 h. The difference between the forecast at 12 h and the corresponding model analysis for this event is slight.

Figure 4 compares the ECMWF 10-m wind at the moving R/V *Melville* location with the wind observed aboard ship. The model wind jumps about as much as the R/V *Melville* wind, but this occurs an hour or two later. Also, because of the coarser resolution, the transition is smoothed over a longer time.

Figure 5 shows the initial weather analysis at midnight and the short-range forecast near midday. The colors indicate the 2-m temperature and the black contour lines the surface pressure. The arrows are proportional to the wind-sea significant wave height and point in the mean direction of the wind sea. Using $F_\zeta(f, \theta)$ for the wave amplitude power spectrum as a function of cyclic frequency and direction, the significant wave height H_S is 4 times the rms wave height, and given by [ECMWF (2015), their Eqs. (6.3) and (6.6)]

$$H_S = 4\sqrt{\int F_\zeta(f,\theta)\, df\, d\theta}. \qquad (1)$$

The reason for choosing to display the wind sea rather than the 10-m winds is that it highlights even better the very quiet phase that existed before the arrival of the cold front over a large area around the array. Wind sea is that part of the sea state that corresponds to waves that are generated by the local wind.

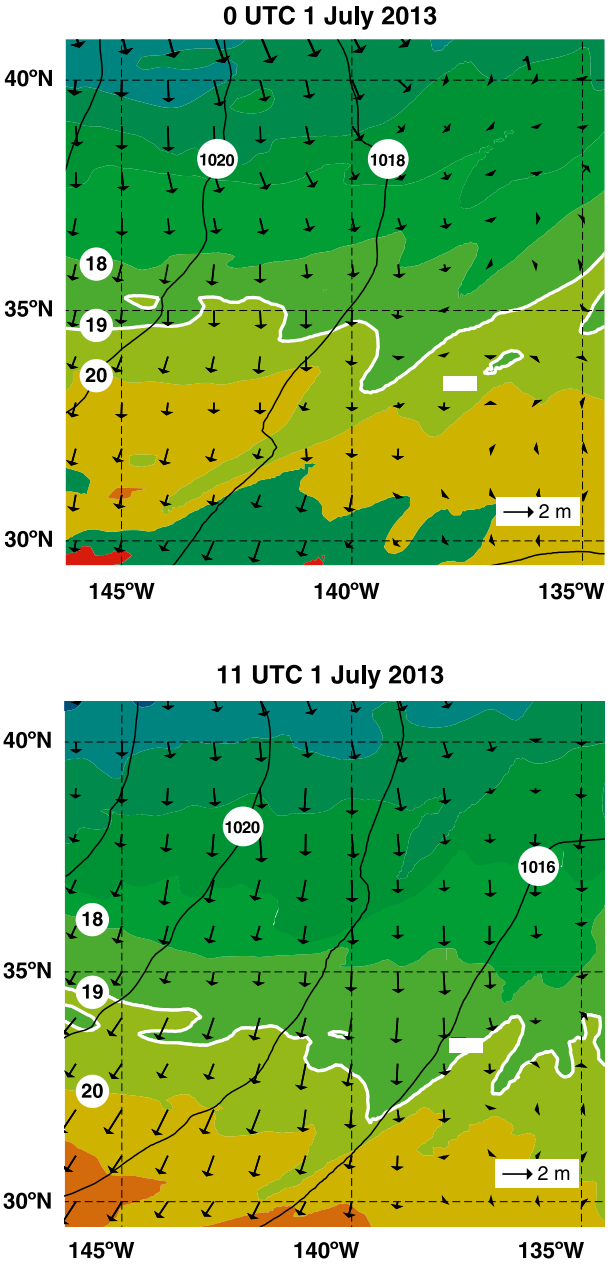

FIG. 5. The passage of the front over OBSANP is clear in the southerly migration of the 2-m temperature (color), as well as the increase in the wind-sea significant wave height (black vectors). The surface pressure (black contours) is less diagnostic. The color shading for the 2-m temperature has 1° steps. The wind-sea arrows are plotted every 1°, much coarser than the 28-km resolution of the model. The white rectangle shows the OBSANP location and is drawn to scale (see Fig. 1). These charts are about 1000 km on a side.

It is not enough to have an overhead wind: it must be large enough to generate and grow wind waves. Because a wave model, such as the one used at ECMWF, contains the details of how the wind is generating waves, it is easy to isolate the wave components that are locally

generated (wind sea) from the waves that have propagated into an area from other sources (swell) (ECMWF 2015). The part of the wave spectrum that contains the wind-sea components is then integrated separately, and an equivalent significant wave height and mean direction can be derived. At 0800 UTC on DOY 182, the significant wave height and period of the wind sea were 0.22 m and 2 s. For the swell, the numbers are 1.7 m and 10 s. The swell was large, but its frequency was well outside our band.

From the sequence in Fig. 5, one can see that, as the wind sea is picking up, the temperature contours move to the south, bringing a 1°–2° fall, just as seen in Fig. 3. The drop in 2-m temperature of the model is less pronounced than the temperature drop observed on R/V *Melville*. The timing of the drop, as well as the increase in wind and wind sea, appear to be about an hour or two later than observed.

Model temperatures correspond to the temperature at the reference height of 2 m above the sea surface and are therefore heavily controlled by the sea surface temperature (SST), which in the ECMWF short-range forecast is kept constant with respect to its initial analysis value. The difference in timing might be due to short-range forecast error and also to smoothing effects that are intrinsic to global numerical weather models. It is, however, worth noting that the passage of the front was not localized to the experiment site but extended over a much larger area surrounding it.

A closer view of the weather at OBSANP around the time of the front's passage is seen in Fig. 6. Here it is the wind-sea H_S that is shown in color, with heights of 0.6 and 0.3 m delineated in white. For the time and place of OBSANP, the heights correspond to 10-m winds of approximately 7 and 5 m s^{-1}, respectively. The black contours show the relative vorticity of the surface wind, with spacing 10^5 s^{-1}. The 5×10^5 s^{-1} isolines are in red.

The two displayed fields are clearly aligned southwest–northeast, with a perpendicular advance toward the southeast. Selected isoline speeds are indicated in Table 1. The estimates were taken along the diagonal. Because of the map distortion, this line is oriented 141°.

It is emphasized that neither of these fields is believed to be a measure of the physical phenomenon generating the acoustic radiation. But they are probably closer to the underlying physical mechanisms than the 10-m wind.

After the passage of the front, the winds remained strong over the array, veering to the northeast following the buildup of a high pressure to the northwest, until the area came under the influence of the remnants of Hurricane Cosme.

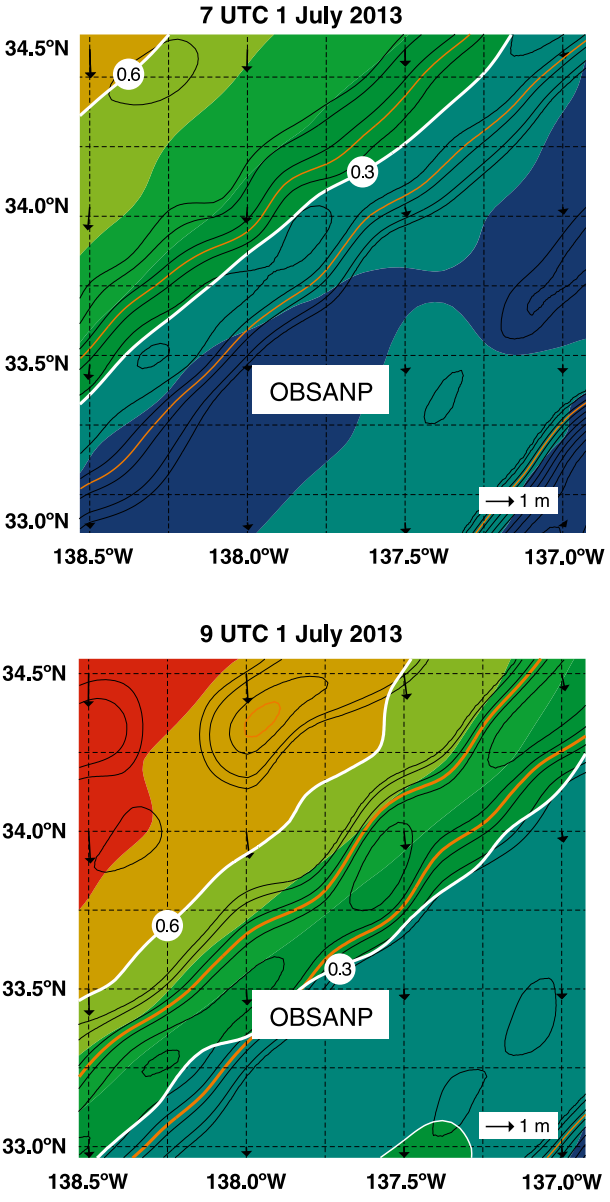

FIG. 6. The contour levels of significant wave height H_S (color) are oriented southwest–northeast. The same alignment is seen in the vorticity within the lowest level of the model (black and red lines). Both fields migrate to the SE during the front's passage. The OBSANP zone (white box) has the same size as the array layout shown in Fig. 1.

3. Data model

The brevity of the jump in acoustics, the differences in spectral level before the jump (see Fig. 2), and the empirical factors needed to equalize the spectra after the jump make accurate estimation of the transition parameters (time of passage and growth rate of the spectrum at passage) challenging. Thus, our approach is to approximate the event by a sigmoid model using the tanh function.

TABLE 1. Speeds, in the direction 141°, of two H_S isolines and one vorticity isoline between 0700 and 0900 UTC, 1 July 2013.

Field	Value	Speed ($m\,s^{-1}$)
H_S	0.6 m	9.3
H_S	0.3 m	6.3
Vorticity	$5 \times 10^5\,s^{-1}$	2.2

The history of the spectrum at any frequency is treated as a time series. In the vicinity of time B, the evolution is parameterized by a time of passage t_0 and spread σ. These parameters are estimated by aligning a tanh function to the amplitude-equalized data. Thus,

$$F_p(f) \approx A\left[\tanh\left(\frac{t-t_0}{\sigma}\right)+1\right]. \qquad (2)$$

Vertical velocity and wind speed are also fit to this functional form. The passage time t_0 measures the hour of the midpoint of the transition. The spread σ measures the rapidity of the change at a station. In the interval $t_0 \pm \sigma/2$, the signal grows from 27% to 73% of its range, almost half the total swing.

The sensors have different noise floors, and using the nominal transfer functions gives different spectrum levels for times just after the front's passage. If each series were fit independently, these differences would influence the constant A, thereby biasing the key parameters t_0 and σ. To ameliorate this, all data were scaled to match the pressure record for LPB (see below) and its A [Eq. (2)] taken for all other channels. This is tantamount to neglecting possible bottom effects and assuming that perfect, noise-free observations would give the same tanh function everywhere, except for the passage time and spread.

The nonlinearity couples the two free parameters, which were adjusted by trial and error. Representative examples are shown in Fig. 7, and Table 2 lists the results. Compared to the R/V *Melville* wind record, the acoustics both leads and lags in time. More interestingly, the spread σ, which measures the speed of transition, is 5 times longer for the acoustic field than the wind driving the physics generating it.

4. Physical model

The weather-associated transition in bottom sound (pressure and vertical velocity) has been reduced to two variables, not counting the empirical amplitude adjustments. Various physical models can be invoked to interpret these parameters.

a. Passage across the array

Take a front heading exactly southeast (135°) and project the station locations onto this direction. Then the moveout (a term we borrow from exploration seismology) is reasonably fit by a front speed of either $10\,km\,h^{-1}$ ($2.8\,m\,s^{-1}$) or twice as fast, $5.6\,m\,s^{-1}$, depending on the significance attached to the data from SP8, the station furthest from the origin (Fig. 8). Incorporating the moveout of the 400-Hz spectra (see below) tends to favor the slower speed.

b. Passage over a station

Sound from the waves behind the front can reach a deep station over three paths. Waves of low enough frequency can outrun the front and, if there is an appreciable overlap integral, radiate sound directly downward before the front's arrival. Sound generated from waves behind the front, by the L-H mechanism, will project energy into the ocean ahead of the front. Finally, it will take time for the waves behind to reach full development (i.e., be in equilibrium with the overhead wind). Some of the acoustic change may be associated with the overhead wave growth after passage.

1) WAVES BEFORE THE FRONT

If the wind behind the front is strong enough and the wind sea fully developed, waves of sufficiently low frequency can outpace the front. For this to be the case, the group velocity, $\partial\omega/\partial\kappa$, must exceed the front velocity v_f (Sverdrup and Munk 1947, their Fig. 3). For wave frequency f_w, this gives

$$f_w < \frac{g}{4\pi v_f}. \qquad (3)$$

Ocean gravity waves of frequency f_w radiate acoustic waves of frequency $f_a = 2f_w$ by the L-H mechanism, provided there is sufficient angular spread to give a significant overlap integral. For $f_a = 4$ Hz, we have $v_f < g/(8\pi) = 0.4\,m\,s^{-1}$. The observed front moved about 10 times faster, which rules out this mechanism.

2) SOUND BEFORE THE FRONT

Sound from the front will arrive at a station before the front passes overhead because an acoustic dipole radiates at all angles into the ocean beneath. This guarantees that a deep enough sensor can see an acoustic signal from the moving dipole arbitrarily earlier than its overhead passage, since the front's speed is so much less than the speed of sound in seawater.

Take the wind behind the front to be the same everywhere and the wind sea fully developed. The rippled ocean may have a spectrum that varies with wavenumber, but assume the spectrum is constant in space and time. Assume the wind sea emits L-H radiation. We are focused on steep rays and neglect the sound speed profile.

Let R be the slant distance from an element of area in the rippled part to a point on the bottom. Let θ be the angle

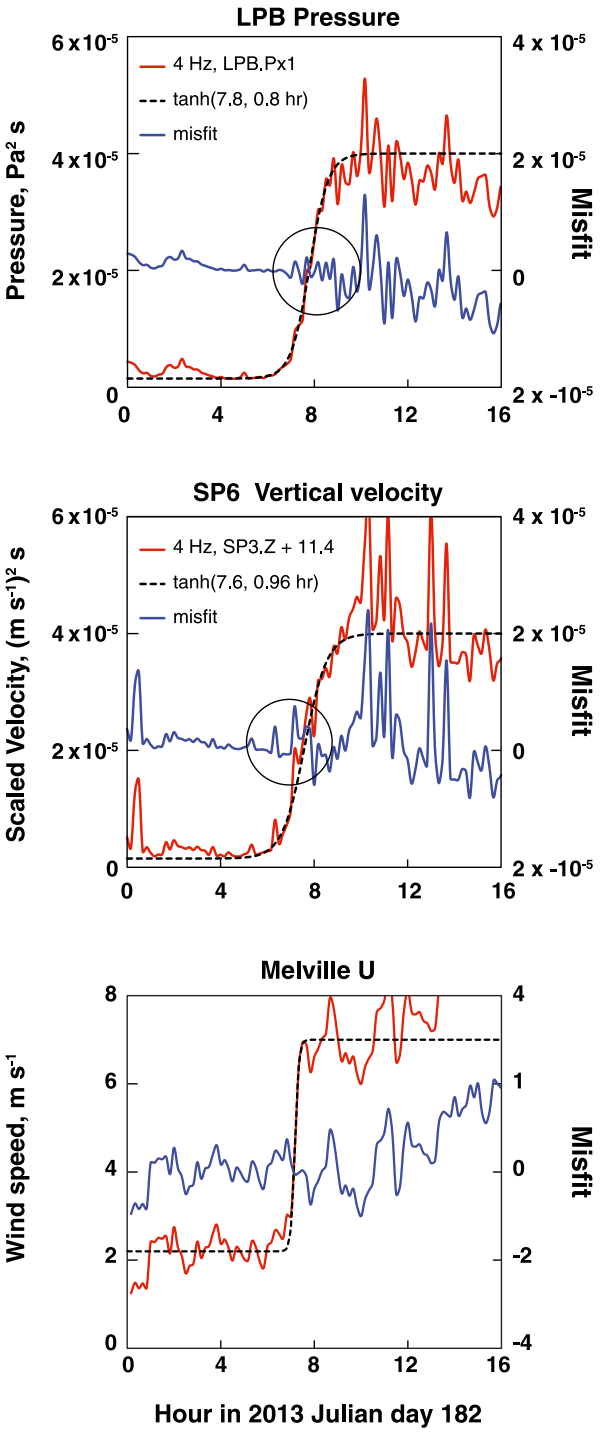

FIG. 7. The tanh approximations to the transitions in (top) pressure, (middle) vertical velocity, and (bottom) wind speed are shown as black dashed lines. The data, in red, are referenced to the linear scale on the left axis. The misfit, in blue, is referenced to the right axis. The critical interval is the zone around the midpoint of the transition, indicated by the circles. (middle) The velocity data have been scaled by 2.6×10^{11}, or 114 dB. The spectrum of vertical velocity at this station and frequency is approximately 16 dB larger than at LPB or LPD but was measured on a different sensor (see Table 5).

TABLE 2. Parameters of tanh model for the 4-Hz spectrum of pressure and vertical velocity. Data from SP8 are excluded from the averages because of the large discrepancy between the onset times of pressure and velocity. SP8 was atop a seamount and 600 m shallower than the other stations. For comparison, fitting the model to the R/V *Melville* wind record gave parameters $t_0 = 7.2$ h and $\sigma = 0.2$ h.

	Pressure		Velocity	
Station	t_0 (h)	σ (h)	t_0 (h)	σ (h)
LPB	7.8	0.8	7.6	0.8
LPD	7.3	0.6	7.2	1.0
SP3	7.6	0.9	7.6	1.0
SP4	7.4	1.0	7.4	0.7
SP5	7.2	1.0	7.5	1.1
SP6	6.9	0.6	7.0	1.0
Mean	7.37	0.82	7.38	0.93
SP8	6.3	1.0	5.0	0.9

the slant distance makes with the vertical and ϕ the horizontal angle with respect to the front. There are four relevant Green functions: G_p for pressure, G_z for vertical velocity, G_x for horizontal velocity normal to the front, and G_y for horizontal velocity parallel to the front. These are

$$G_p = \left(\frac{\cos\theta}{R}\right)^2, \tag{4}$$

$$G_z \propto \cos^2\theta\left(\frac{\cos\theta}{R}\right)^2, \tag{5}$$

$$G_x \propto \cos^2\phi\sin^2\theta\left(\frac{\cos\theta}{R}\right)^2, \quad \text{and} \tag{6}$$

$$G_y \propto \sin^2\phi\sin^2\theta\left(\frac{\cos\theta}{R}\right)^2. \tag{7}$$

In the Green functions for velocity, and for a homogeneous and unbounded fluid medium, the proportionality constant is Z^{-2}, with $Z = \rho c$ the acoustic impedance. This is approximately true when the sensor is a seismometer emplaced on the elastic sea floor.

Normalize all lengths by the observation depth (in this case the ocean bottom), and let x $(-\infty < x < \infty)$ be the front's position. The speed of sound is assumed infinite. The bottom spectra at the origin for unit dipole strength per unit area are then

$$F_p = \frac{\pi}{2}\left[1 + \frac{x}{(x^2+1)^{1/2}}\right], \tag{8}$$

$$F_z = \frac{\pi}{4Z^2}\left[1 + \frac{x^3 + 1.5x}{(x^2+1)^{3/2}}\right], \tag{9}$$

$$F_x = \frac{\pi}{8Z^2}\left[1 + \frac{x^3}{(x^2+1)^{3/2}}\right], \quad \text{and} \tag{10}$$

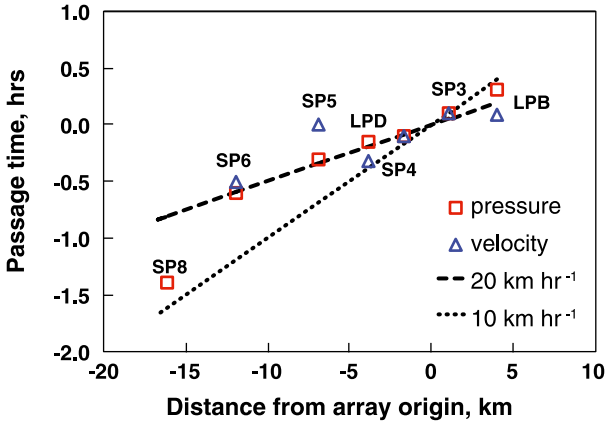

FIG. 8. The passage times for the 4-Hz pressure and vertical velocity, as a function of the distance normal to the front, indicate speeds between 10 and 20 km h^{-1} (2.8–5.6 m s^{-1}). For SP8 (−16 km), the passage time for vertical velocity is −2.5 h, which falls outside the plot range. The times in Table 2 have been shifted by 7.5 h, so zero hour occurs at the array origin.

$$F_y = \frac{\pi}{8Z^2}\left[1 + \frac{x}{(x^2+1)^{1/2}}\right] = \frac{F_p}{4Z^2}. \qquad (11)$$

For $x = +\infty$, an ocean covered by random acoustic dipoles, the far-field pressure is π times the dipole density, a standard result (Wilson 1983).

The source model leading to Eqs. (8)–(11) is a half-plane of incoherent acoustic dipoles with a step transition at the leading edge. As the front advances, this gives the quickest possible change with time of the bottom acoustics. If the front's leading edge has a gradual rise, the acoustic change happens more slowly.

Figure 9 shows two cases. The top panel is for the step change front, the bottom panel the case where a two-unit linear transition strip precedes the front. For the step-change front, the acoustic variation is concentrated over a horizontal span about equal to the observation depth, and the midpoint occurs with the front exactly overhead. For the front with a linear transition (bottom), the halfway point in the acoustic transition occurs when the middle of the transition strip is overhead, but the front (defined as the position at which the acoustic source reaches full intensity) is still to the left.

In both cases, the change is faster for velocity (red) than for pressure (blue). This is a consequence of the $\cos^2$ factor in the Green function for vertical velocity [see Eq. (5)]. However, this discrepancy is reduced when the front is gradual.

The analytic solutions are reasonably fit by tanh functions (Fig. 9; Table 3). For fitting, the vertical velocity is scaled according to

$$F_z' = Z^2 F_z. \qquad (12)$$

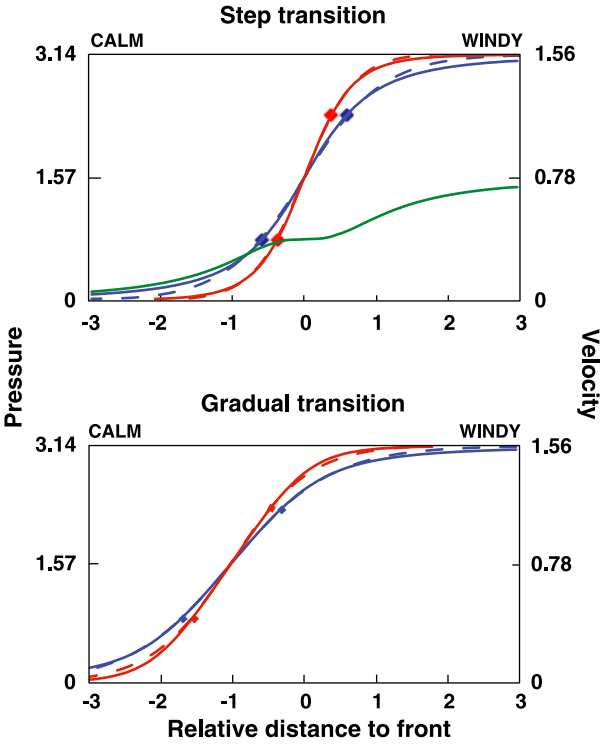

FIG. 9. (top) The acoustic radiation from a dipole half-layer with step transition at the leading edge changes more quickly with position than (bottom) from a layer preceded by a two-unit transition strip. The change in vertical velocity (red, right axis) as the front advances is steeper than the change in pressure (blue, left axis), but the difference is less for (bottom) the front with the gradual transition. The dashed curves are tanh approximations to the analytic solutions. The diamonds span one normalized spread length σ, centered on the transition midpoint. The horizontal velocity perpendicular to the front in (top) (green, right axis) has an inflection at the time of passage, the least overall range, and no resemblance to a sigmoid function. Velocity parallel to the front is a scaled version of the pressure response [Eq. (11)].

This sets $F_z'(\infty) = \pi/2$, as seen in the right axes of the figure.

3) SPEED FROM GROWTH RATE

The ratio of the model's spread parameters with respect to distance (see Fig. 9) to the measured acoustic spread parameters with respect to time σ, gives an apparent speed for the front's passage over the measurement location. Taking $\sigma_p = 0.82$ h and $\sigma_z = 0.93$ h as averages for the data (see Table 2), an observation depth of 5000 m, and the linear transition model (Table 3) gives the following two estimates:

$$v_{\text{front}} = \frac{1.4 \times 5000}{0.82 \times 3600} = 2.37 \text{ m s}^{-1} \text{ from pressure; and} \qquad (13)$$

TABLE 3. Parameters of the tanh fit to the two acoustic source models. The units are relative distance (see Fig. 9).

	Step transition			Linear transition		
	P	V	σ_p/σ_v	P	V	σ_p/σ_v
x_0	0	0		−1.0	−1.0	
σ	1.1	0.7	1.57	1.4	1.1	1.27

$$v_{\text{front}} = \frac{1.1 \times 5000}{0.93 \times 3600} = 1.64\ \text{m s}^{-1}\ \text{from vertical velocity}. \tag{14}$$

If the model with a step change in the dipole layer is taken, the spreads would be smaller. This would yield 30% lower speed estimates, in greater conflict with the moveout analysis and weather model.

The speed from the pressure growth rate (equivalent to 8.5 km h^{-1}) is not far from the 10 km h^{-1} approximation to the data shown in Fig. 8 (and below in Fig. 13). The speed from the vertical velocity spectrum at 4 Hz is significantly less than the other estimates. This is because the measured spread in time is larger than pressure's (Table 2), whereas theory would have it smaller (Table 3). The discrepancy between velocity data and model is reduced when the front has a linear transition at the leading edge but is not eliminated.

5. High frequencies

The AB bust in days 181–182 was even stronger at 400 Hz than at 4 Hz; 21 dB versus 14 (Fig. 10). As with the lower frequency, the spectra for the interval around time B vary with location, the rise being earlier in the west than the east. Similarly, the jump in acoustics is much slower than the jump in wind speed.

It is notable that, whereas the 4-Hz spectrum varies little under strong winds, the 400-Hz spectrum follows its fluctuations even when $U \gtrsim 6\ \text{m s}^{-1}$. These differences are seen in the record for the middle two weeks of the experiment in Figs. 2 and 10. The difference is particularly clear around label A. The 4-Hz pressure is flat up to A, and then declines precipitously. The 400-Hz pressure begins its fall into the bust a day before A, accurately following the wind.

The reference frequency was chosen to be 400 Hz because frequencies even a little lower are susceptible to contamination by R/V *Melville* interference. The ship's radiation is easily seen, even at a distance of 50 km, when the wind is low. A little past time A, ship noise dominates the acoustic signal at this frequency, so the descent into the bust is masked. However, the passage of the front, causing the bust to end, gives striking results (Fig. 11).

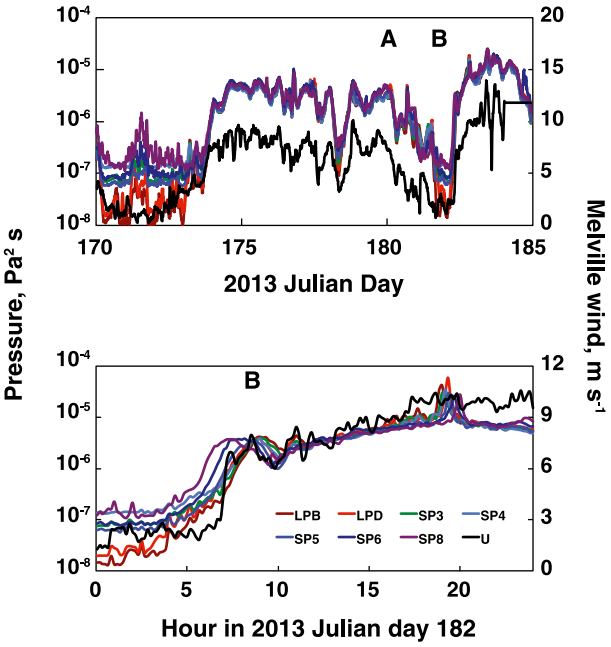

FIG. 10. Spectral estimates of pressure for (top) 4 Hz and (bottom) 400 Hz. The 400-Hz spectral estimates of pressure follow the wind more closely than the 4-Hz estimates (see Fig. 2). For example, the dip in wind near day 178 is correlated to a much deeper dip in the 400-Hz spectrum than the 4-Hz spectrum. The color scheme, shown in the legend for 400 Hz, is the same as used in Fig. 2. As before, the best sensors (LPB, dark red; LPD, red) have lower self-noise than the HTI-90-U. The wind in (top) is smoothed over 1 h, and in (bottom) 10-min smoothing was applied.

The figure shows spectra of bottom pressure for three brief data windows at stations 15 km apart, measured in the direction of the front's motion. Windows for LPB (solid) are delayed exactly 1 h from the windows for SP3 (dashed). Thus, each pair of spectra are for windows at comparable phases of the acoustic response to the passage of the front. The similarity is further support for the hypothesis that the acoustic source function associated with the front was merely advected over the array with little change as it progressed.

The number to the right of each pair of spectra is an estimate of the wind overhead. It was calculated as follows. Figure 10 shows that, for most of the time, the 400-Hz spectral estimate and the R/V *Melville* wind move together, even though R/V *Melville* was in constant motion, often tens of kilometers from the array. Analysis of the correlation supports a linear relationship between the logarithm of the spectrum and the wind speed in meters per second. Specifically,

$$10 \log F_p \approx -78 + 3U. \tag{15}$$

The slope, 3 dB s m^{-1}, is close to the value that may be inferred from spectra from a deep hydrophone at

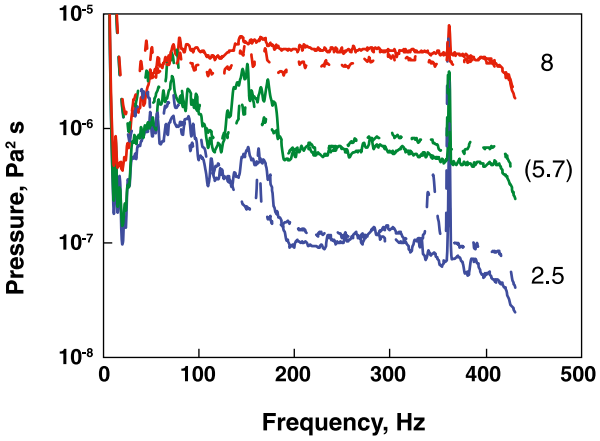

FIG. 11. The high-frequency spectra at LPB (solid) and SP6 (dashed) are relatively flat and similar at matching points in the front's passage. The front arrived earliest at SP6, and its spectra, for 10-min windows, are centered on 0318, 0624, and 0800 UTC 1 July 2013, for a total span of 4.7 h. The LPB spectra are for windows exactly 1 h later, the appropriate delay for the speed of passage (see Fig. 13). The narrow ($\delta f \approx 1$ Hz) peak at 360 Hz is radiation from R/V *Melville*, as are the broad humps centered on 75 and 150 Hz. The numbers on the right are estimated overhead wind speeds ($m\,s^{-1}$) (see text).

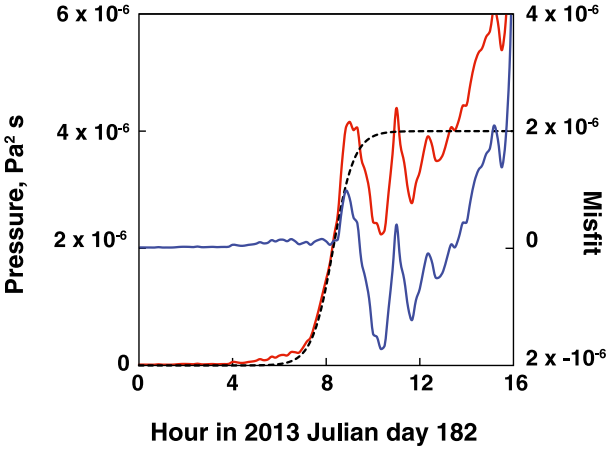

FIG. 12. The tanh approximation to pressure for the 400-Hz spectrum from LPB is similar to the 4-Hz fits (cf. Fig. 7). The spectrum (red) is referenced to the left axis, the misfit (blue) to the right axis.

Aloha Cabled Observatory (ACO), north of Hawaii (Duennebier et al. 2012). At 24 Hz, Farrell and Munk (2010, their Fig. 5) estimated a gradient of 2 dB s m^{-1} for data from the Hawaii-2 Observatory (H2O).

Equation (15) is applied to this particular event with caution. Most of the data behind Eq. (15) were taken at times when the wind field was slowly changing and presumably homogeneous over the array and beyond. From this, we infer that the acoustic field excited by the wind was also homogeneous. For the blue spectra, taken just as the front was approaching, and the red spectra, taken after it had passed, it is reasonable to assume a homogeneous source field overhead. In this case, it is legitimate to apply Eq. (15) to infer the wind speed from the measured spectrum. Indeed, these speeds are not very different from the wind recorded on R/V *Melville*.

For a time in the middle of the transition (green), however, the acoustic source field is assuredly not homogeneous, because the edge of the front is over the station, with relatively calm seas ahead and windy seas behind. Therefore, the wind speed derived from Eq. (15) is shown in parentheses.

A representative example of the tanh fits at high frequencies is given in Fig. 12. Table 4 shows the results of fitting this function to the pressure records of the 400-Hz spectral estimates. The passage times, assuming a front directed toward 135°, favor the 10 km h^{-1} assumption for the speed of advance (Fig. 13). For most stations, the passage time at 400 Hz is about 25 min later than the 4-Hz time. On the other hand, the spreads are about an hour at both frequencies.

6. Discussion

The OBSANP deployment gave a unique opportunity to observe the acoustic signature of a weather front passing over an array on the deep Pacific sea floor. Our original objective, using bottom acoustics to study the growth of a wind sea overhead, is only partially realized. It has been shown that the data support a model in which the acoustic sources build up linearly over a distance of order 10 km before reaching full strength. At the lower frequency, 4 Hz, the source is well modeled as L-H radiation so that in the transition zone it is the quantity $F_\zeta^2 I$ that is increasing, not just the wave spectrum itself.

This study shows the merits of joining assimilated weather models, numerical wind-sea models, and deep ocean acoustics. Future experiments of this type should expand on this collaborative approach. Wind-sea modeling could easily be extended beyond the present limit of 1 Hz. Other weather patterns could be revealing.

a. *High frequencies*

The response to the front's passage at high frequencies (400 Hz) is about as rapid (1 h) as the response at low frequencies (4 Hz), but delayed in time by about 25 min. Since the physics behind the acoustic signal at this frequency is definitely not L-H radiation, there is no reason the times should match.

X. Zabalgogeazcoa (2009, personal communication), analyzed spectra for frequencies between 20 and 400 Hz during a small weather front present in Church Opal

TABLE 4. Parameters of tanh model for the 400-Hz spectrum of pressure. The velocity data were unusable at this frequency.

Station	t_0 (h)	σ (h)
LPB	8.3	0.9
LPD	7.9	1.1
SP3	8.1	1.0
SP4	8.1	1.0
SP5	7.6	1.0
SP6	7.0	0.8
Mean	7.8	1.0
SP8	6.3	0.6

data (Gaul et al. 2007). He found that the high-frequency signature was about 15 min earlier than the low-frequency signature.

b. Vertical velocity

The passage time at a station of vertical velocity is about the same as for pressure, and the array averages are identical (Table 2). Unlike the model, the measurements of the spread in the vertical velocity are also nearly identical to those of pressure. The model with a sharp front would have velocity rising 1.5 times faster than pressure at passage, and this theoretical ratio is lowered to 1.3 with the 10-km transition zone. Given the consistency across the stations, the relatively slow rise in velocity is real and at variance with the model.

c. Horizontal velocity

A few spectra of data from the horizontal seismometers have been examined, and, for frequencies near 4 Hz, the time evolution of the power is similar to that of the vertical seismometer. Because the direction of the front's approach is poorly known and because the orientation of the instruments is unknown, it is not possible to rotate the measured components to search for the inflection in the response of the horizontal velocity in a direction parallel to the front (see Fig. 9).

Thus, the signal that is seen will be a mixture of components perpendicular, F_x [Eq. (10)], and parallel, F_y [Eq. (11)], to the front. The inflection in the parallel component is diagnostic, but since the signal is low, it will likely be swamped by the projection of the perpendicular component.

In principle, the directions of the axes could be found from analysis of earthquake arrivals. However, to use this information would require accurate knowledge of the front's orientation. In general, this will be unknown. A better approach might be to search for the front's direction by rotating the seismic components to achieve a separation that yields one component with a small time derivative at the time of passage. Even this approach would fail unless the front was straight and linear out to a few observation depths each side.

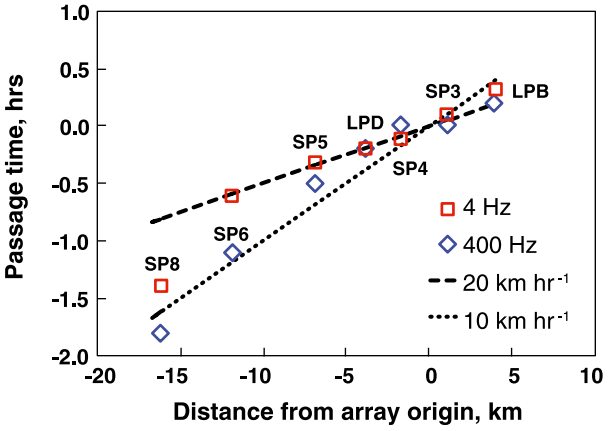

FIG. 13. The passage time for the 400-Hz pressure spectrum (blue diamonds) indicates a front speed close to 10 km h^{-1}. This hinges on the large difference between the passage time estimated from 4 Hz (red squares) and 400 Hz for station SP6 at −12 km. For this plot, the 400-Hz passage times in Table 4 have been shifted by 8.1 h, so the time is 0 at the array origin.

d. Spectrum equalization

The acoustic model envisages a bottomless ocean with constant sound speed. If an elastic sea floor consisting of plane parallel layers were to be incorporated, there would be only a small effect on the model response (Fig. 9) because over the critical range interval, $\pm 1 \times$ observation depth, all rays are nearly vertical.

The real bottom is more complex, and there are expected to be variations in the coupling of the sensing systems to the ocean sediments. These effects are evident in the variations of the velocity spectra from location to location.

However, at any one frequency, these are taken to give constant offsets in the spectra, which will not be altered by the variable acoustic field generated at the ocean surface above. Thus, for the reasons given above, empirical factors (see Table 5) have been introduced to equalize the 4- and 400-Hz spectra.

The nominal 400-Hz spectra of data from the sensors at LPB and LPD were raised 9.5 dB. From analysis of spectra from these sensors and the HTI-90-U on the SP stations, we inferred the nominal transfer function of the SAIC hydrophone incorporated an extraneous pole at 180 Hz. Figures 10 and 11 show how well the elimination of this pole aligns the signals of the two transducers.

For the pair of sensors at LPB, the spectral ratio $F_p(4)/F_v(4) \approx 1.2 \times 10^{13}$ (131 dB). With this as the baseline, the other velocity data were equalized with the adjustments shown in the middle row of Table 5.

TABLE 5. The following scale factors were applied to equalize the spectra. Units are in decibels, so for row 1, for instance, the tabulated quantities are $10\log[F_0/F_{\mathrm{LPB}}]$. The velocity factors are with respect to 131 dB (1.2×10^{13}), which equalizes the two data types at LPB.

Station	Pressure, 4 Hz	Velocity, 4 Hz	Pressure, 400 Hz
LPB	0.0	0.0	0.0
LPD	−1.9	10	0.0
SP3	0.0	−16	1.6
SP4	0.5	−17	1.6
SP5	−1.3	−17.5	1.5
SP6	−5.4	−24	1.8
SP8	−1.0	−33	1.8

Figures 2 and 7 illustrate the efficacy of this impedance-like transformation. For seawater, $Z^2 = 123.5$ dB is the squared impedance.

Acknowledgments. Our interest in abrupt changes in bottom acoustics was first triggered by the work of Charles Peureux during a 2014 summer visit to Scripps. Bertrand Chapron and Fabrice Ardhuin, also of IFREMER, have offered insights. We thank the SIO OBS Instrument Program, and E. Aaron in particular, for their support. The OBSANP cruise was funded by the Office of Naval Research under Grants N00014-10-1-0987, N00014-14-1-0324, N00014-10-1-0510, and N00014-10-1-0990.

REFERENCES

Brekhovskikh, L. M., 1966: Underwater sound waves generated by surface waves in the ocean. *Izv. Acad. Sci. USSR, Atmos. Oceanic Phys.*, **2**, 970–980.

Deane, G. B., and M. D. Stokes, 2010: Model calculations of the underwater noise of breaking waves and comparison with experiment. *J. Acoust. Soc. Amer.*, **127**, 3394–3410, doi:10.1121/1.3419774.

Dorman, L. M., A. E. Schreiner, L. D. Bibee, and J. A. Hildebrand, 1993: Deep-water sea-floor array observations of seismo-acoustic noise in the eastern Pacific and comparisons with wind and swell. *Natural Physical Sources of Underwater Sound, Sea Surface Sound (2)*, B. R. Kerman, Ed., Kluwer Academic Publishers, 165–174, doi:10.1007/978-94-011-1626-8_14.

Duennebier, F. K., R. Lukas, E. Nosal, J. Aucan, and R. Weller, 2012: Wind, waves, and acoustic background levels at Station ALOHA. *J. Geophys. Res.*, **117**, C03017, doi:10.1029/2011JC007267.

ECMWF, 2015: CY41R1 official IFS documentation. Accessed April 2016. [Available online at https://software.ecmwf.int/wiki/display/IFS/CY41R1+Official+IFS+Documentation.]

Farrell, W. E., and W. Munk, 2010: Booms and busts in the deep. *J. Phys. Oceanogr.*, **40**, 2159–2169, doi:10.1175/2010JPO4440.1.

——, and ——, 2013: Surface gravity waves and their acoustic signatures, 1–30 Hz, on the mid-Pacific sea floor. *J. Acoust. Soc. Amer.*, **134**, 3134–3143, doi:10.1121/1.4818780.

Gaul, R. D., D. P. Knobles, J. A. Shooter, and A. F. Wittenborn, 2007: Ambient noise analysis of deep-ocean measurements in the northeast Pacific. *IEEE J. Oceanic Eng.*, **32**, 497–512, doi:10.1109/JOE.2007.891885.

Goncharov, V. V., 1970: Sound generation in the ocean by the interaction of surface waves and turbulence. *Izv. Atmos. Ocean. Phys.*, **6**, 1189–1196.

Guralnik, Z., X. Zabalgogeazcoa, J. Bourdelais, and W. E. Farrell, 2013: Wave–wave interactions and deep ocean acoustics. *J. Acoust. Soc. Amer.*, **134**, 3161–3173, doi:10.1121/1.4818782.

Hasselmann, K., 1963: A statistical analysis of the generation of microseisms. *Rev. Geophys.*, **1**, 177–210, doi:10.1029/RG001i002p00177.

Janssen, P. A. E. M., 2008: Progress in ocean wave forecasting. *J. Comput. Phys.*, **227**, 3572–3594, doi:10.1016/j.jcp.2007.04.029.

Knudsen, V. O., 1948: Underwater ambient noise. *J. Mar. Res.*, **7**, 410–429.

Longuet-Higgins, M. S., 1950: A theory of microseisms. *Philos. Trans. Roy. Soc. London*, **A243**, 1–35, doi:10.1098/rsta.1950.0012.

McCreery, C. S., F. K. Duennebier, and G. H. Sutton, 1993: Correlation of deep ocean noise (0.4–30 hz) with wind, and the Holu spectrum—A worldwide constant. *J. Acoust. Soc. Amer.*, **93**, 2639–2648, doi:10.1121/1.405838.

Oguz, H. N., 1994: A theoretical study of low-frequency oceanic ambient noise. *J. Acoust. Soc. Amer.*, **95**, 1895–1912, doi:10.1121/1.408704.

Stephen, R. A., and Coauthors, 2014: Ocean Bottom Seismometer Augmentation in the North Pacific (OBSANP)—Cruise report. Woods Hole Oceanographic Institution Tech. Rep. WHOI-2014-03, 241 pp., doi:10.1575/1912/7130.

Sverdrup, H. U., and W. H. Munk, 1947: Wind, sea, and swell: Theory of relations for forecasting. U. S. Hydrographic Office Tech. Rep. 1, 36 pp.

Wilson, J. D., and N. C. Makris, 2006: Ocean acoustic hurricane classification. *J. Acoust. Soc. Amer.*, **119**, 168–181, doi:10.1121/1.2130961.

Wilson, J. H., 1983: Wind-generated noise modeling. *J. Acoust. Soc. Amer.*, **73**, 211–216, doi:10.1121/1.388841.